

# Exoplanet characterization based on nulling interferometry

Evaluation of suitable exoplanet candidates for a test mission with the goal of showing  
feasibility of space-based nulling interferometry

Philipp Binkert

December 26, 2021

## Abstract

Space-based nulling interferometry a promising concept to spectrally characterize the atmospheres of Earth-like exoplanets. This report examines whether it is possible to show the feasibility of this concept by confirming exoplanets that have previously been detected using direct imaging methods using small CubeSat (6U and 12U) or medium-sized PROBA telescopes. To this end, a model is created that calculates the various incoming fluxes that constitute the total incoming signal and determines whether the signal-to-noise ratio is sufficient for the exoplanet to be observed. The results show that many of the planets considered can indeed be detected using this setup. The model is validated by comparing its results to those of an independently created model by Colin Dandumont et al. To fully demonstrate the feasibility of the proposed mission, some neglected sources of flux such as exozodiacal dust as well as the exact geometry of the telescopes should be included in further research on the topic.

## Contents

<b>1</b>	<b>Introduction</b>	<b>2</b>
<b>2</b>	<b>Model</b>	<b>3</b>
2.1	Telescopes . . . . .	3
2.2	Incoming signals . . . . .	4
2.3	Noise contributions . . . . .	6
2.4	Signal-to-Noise ratio and integration time . . . . .	7
<b>3</b>	<b>Results</b>	<b>7</b>
3.1	Overview . . . . .	7
3.2	Differences between configurations . . . . .	9

3.3	Impact of platform stability constraints . . . . .	10
<b>4</b>	<b>Discussion</b>	<b>10</b>
4.1	Incoming fluxes . . . . .	10
4.2	Results for nearby exoplanets . . . . .	12
4.3	Results for directly imaged exoplanets . . . . .	12
<b>5</b>	<b>Conclusion</b>	<b>13</b>
	<b>Appendices</b>	<b>15</b>
	<b>References</b>	<b>20</b>

# 1 Introduction

In the past 25 years, over 4200 exoplanets have been detected, the vast majority of them using transit and radial velocity methods. While these findings have provided evidence that planetary systems are indeed common throughout our galaxy, the fact that these two methods only indirectly reveal the exoplanets has its limitations. Direct imaging would allow us to additionally spectrally characterize their atmospheres and search for signs of extraterrestrial lifeforms.

Direct imaging of exoplanets is extremely difficult however, due to the small angular separation between the star and the planet and the huge difference in magnitude. The most promising method to tackle this challenge is based on nulling interferometry or, more specifically, a Bracewell interferometer, which will be the concept analyzed in this report. The basic principle of a Bracewell interferometer consists of two apertures, whereby the light passing through one of them undergoes a phase delay of  $\pi$  before recombination. The apertures are aligned such that the object which is to be suppressed (in this case the star) lies exactly on the axis between the apertures, as this light interferes completely destructively due to the phase shift. The exoplanet on the other hand (given that it is not also directly in the line of sight) is slightly off-axis and thus there is a slight optical path difference between the paths taken to the two apertures. For certain angles, this optical path difference will exactly compensate for the phase shift before recombination, resulting in constructive interference for the exoplanet. See Figure 1 for a schematic drawing of a Bracewell interferometer and the resulting fringe pattern.

There exist already several ground-based telescopes using the Bracewell concept (e.g., the Large Binocular Telescope Interferometer [2]). To avoid atmospheric effects and achieve the desired precision however, a space-based mission is required. This is the goal of the Large Interferometer for Exoplanets (LIFE) mission, which has the objective of characterising the atmospheres of dozens of extraterrestrial planets at mid-infrared wavelengths to assess their potential habitability ([3]).

The costs of such a mission are undoubtedly very high. In order to demonstrate the feasi-

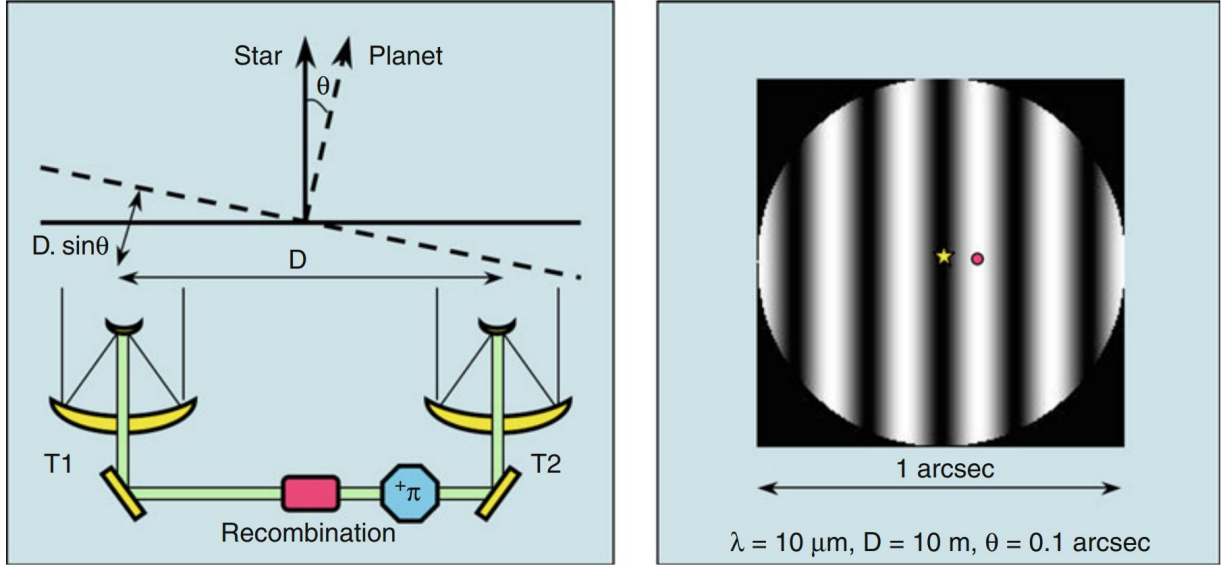


Figure 1: Schematic setup of a Bracewell interferometer (left); two apertures are directed at the system of interest and the light coming from one of the apertures induces a phase-shift of  $\pi$  before recombination. This leads to the fringe pattern depicted on the right (image from [1]).

bility of the nulling interferometry technique in the conditions of outer space, a preceding smaller mission is desirable. The aim of this report is to analyse whether exoplanets from the Nasa Exoplanet Archive ([4]) that have previously been detected using other direct imaging methods could be seen using a small Bracewell interferometer. If so, such a mission could serve as a proof of concept and thereby lay the foundation for the LIFE mission.

## 2 Model

In this section I first introduce the satellite configurations considered. Then I describe the signals and noises contributing to the radiometric budget and which of them are accounted for in my model. Finally, the calculation of the signal-to-noise ratio will be presented.

### 2.1 Telescopes

The three satellite configurations considered are listed in Table 1. The relevant parameters are the baseline (distance between the two apertures), the pupil diameter and the optical train temperature. CubeSats are built up of multiple units, whereby one unit is a block of  $1\text{U} = 0.1 \times 0.1 \times 0.1\text{m}$ . The PROBA-size satellite is larger and has deployable arms, which allows it to achieve a baseline length of 5m. The functioning principle of all the satellites is the same: The elements in the optical path are two lenses, mounted on the same structure and spaced by the baseline length, tip/tilt mirrors to correct any errors, optical delay lines

	<b>CubeSat 6U</b>	<b>CubeSat 12U</b>	<b>PROBA</b>
Dimensions	0.6 x 0.1 x 0.1m	1.1 x 0.1 x 0.1m	1m <sup>3</sup>
Baseline length b	0.5m	1m	5m
Pupil diameter D	0.08m	0.08m	0.25m
Optical train temperature	150K	150K	100K

Table 1: The three satellite configurations considered in this report

to correct the optical path differences (OPD), a fiber injection system to filter the signal, an achromatic phase shifter ( $\pi$  delay in one arm), the beam combiner to receive the light from both apertures and create interference in the pupil plane, and two photodiodes, one at the constructive output and one at the destructive output (see [7] for a more detailed explanation of the setup).

## 2.2 Incoming signals

The instruments detect photons from the following sources (Figure 2):

- *Stellar flux.* While most of the stellar flux will be suppressed due to the nature of nulling interferometry, some part of it will reach the detector due to the finite angular width of the star. The star is assumed to emit as a perfect black body. The stellar flux per unit wavelength is therefore simply

$$F_{\star}(\lambda) = \frac{\pi R_{\star}^2}{d^2} B_{\lambda}(T_{\star}) \quad (1)$$

with  $R_{\star}$  the stellar radius,  $d$  the distance Earth-star and  $B_{\lambda}$  the blackbody function.

- *Planetary flux.* The incoming planetary flux is the sum of two contributions: the thermal flux, which is induced from the planet's equilibrium temperature under the blackbody assumption, and the reflected flux from the star, which is calculated as the product of the planet albedo and the stellar flux. In total, the flux per unit wavelength is given by

$$F_p(\lambda) = A_b \frac{\pi R_{\star}^2}{d^2} B_{\lambda}(T_{\star}) \Phi(\Theta) \frac{R_p^2}{4a^2} + \frac{\pi R_p^2}{d^2} B_{\lambda}(T_p) \quad (2)$$

with  $A_b$  the wavelength independent Bond-albedo and  $a$  the distance of the exoplanet to its star.  $\Phi(\Theta)$  is a phase function that accounts for the fact that depending on the planets exact position, we receive anywhere from none to all of the reflected light. My model will assume that the planet is at a right angle with respect to the axis earth-star and take  $\Phi(\Theta) = 0.5$ .

- *Local zodiacal emission.* Local zodiacal dust is the dust located inside our solar system. It scatters the light of the star and exoplanet as well as emitting light itself

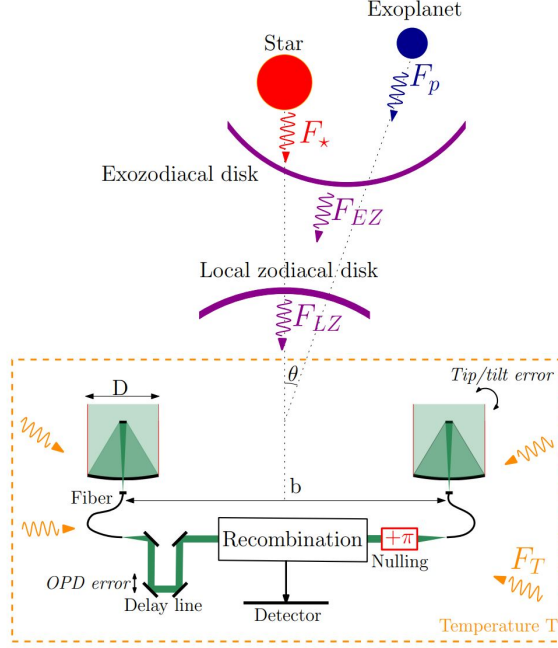


Figure 2: Schematic overview of all incoming fluxes. The contribution from the exozodiacal disk is omitted in this analysis (image from [5]).

in the mid-infrared range. My simulation uses the DarwinSim model ([6]), which describes the emitted flux as a function of wavelength and the position in the sky:

$$F_{zodi}(\lambda, \lambda_{rel}, \beta) = \tau \left[ B_{\lambda}(\lambda, T_{eff}) + A \cdot B_{\lambda}(\lambda, T_{\odot}) \left( \frac{R_{\odot}}{1.5 \text{ AU}} \right)^2 \right] \cdot \left[ \frac{\pi / \arccos(\cos(\lambda_{rel}) \cos(\beta))}{\sin^2(\beta) + 0.36 \cdot \left( \frac{\lambda}{11 \mu\text{m}} \right)^{-0.8} \cos^2(\beta)} \right]^{1/2} \quad (3)$$

where  $\lambda$  is the wavelength,  $\lambda_{rel}$  is the ecliptic longitude relative to the Sun,  $\beta$  is the ecliptic latitude,  $\tau = 4 \cdot 10^8$  is the optical depth towards the ecliptic poles,  $T_{eff} = 265 \text{ K}$  is the effective temperature at 1 AU,  $T_{\odot} = 5778 \text{ K}$  is the effective temperature of the Sun,  $A = 0.22$  is the near-IR dust albedo, and  $R_{\odot}$  is the radius of the Sun. Figure 3 shows a plot of this function for  $\lambda = 5 \mu\text{m}$ . As is reasoned in [6], the effects of scattering from the zodiacal dust can be neglected in the mid-infrared range.

- *Exozodiacal dust emission.* Zodiacal dust is not unique to our solar system. Exozodiacal disks are assumed to be present in most exoplanetary systems and similarly emit and scatter radiation. These effects will not be considered in this analysis due a lack of data for all the regarded systems, but this must certainly be kept in mind during the discussion of the results.
- *Instrumental background flux.* The telescopes and the optical train radiate energy

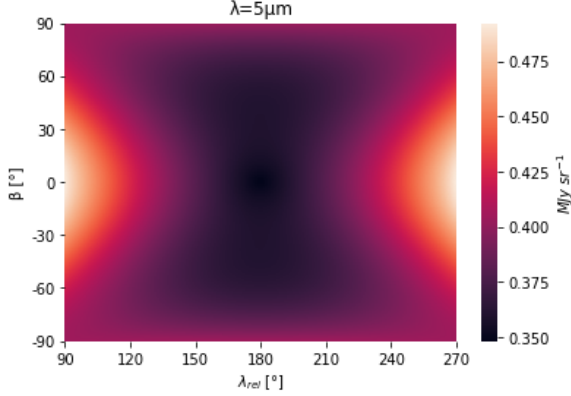


Figure 3: Radiation emitted by zodiacal dust as a function of celestial coordinates at  $\lambda = 5\mu m$ .

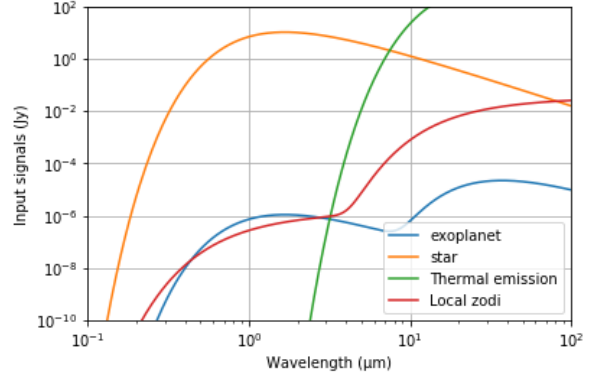


Figure 4: Incoming flux densities for a synthetic planet around Proxima Centauri for  $D = 1m$  and  $T_{instr} = 150K$ .

themselves that must be taken into account. To properly model this contribution, the exact geometry of the telescopes would have to be considered. This exceeds the scope of this analysis; as a simplification, I assume all the instruments to radiate as grey bodies with an emissivity of 0.25 and take a factor of  $10^{-5}$  to account for the geometry (this factor is chosen to match the resulting curve with Figure 3 from [7]).

- *Earth and sun.* The telescope will be directed in such a way that no light from the sun or Earth will enter the apertures.

All of the measured fluxes are depicted in Figure 4 for a synthetic planet around Proxima Centauri (see [5] for its parameters).

Not all of the incoming photons are actually detected. The reflectance of the mirrors, the fiber coupling efficiency and the quantum efficiency of the detector all lead to wavelength dependent losses. My model assumes the instrumental throughput to be 50% at  $0.5\mu m$ , 30% at  $30\mu m$  and linear in between (in accordance with [7]).

## 2.3 Noise contributions

There are two noise contributors that disturb the planet signal, the shot noise  $N_s$  and the instrumental noise  $N_{inst}$  (possible detector noise is not considered in this analysis).

Shot noise is noise due to the incoming signals. It can be described as

$$N_s = \sqrt{\text{OPF} + \text{OBF} + \text{OSF}}, \quad (4)$$

where OPF is the Output Planet Flux, OSF the Output Stellar Flux and OBF the Output Background Flux. The OPF is simply the flux received from the exoplanet as described in section 2.2. The OBF is the sum of the contributions from the zodiacal dust emission and the instrumental thermal emission. The OSF is the the total stellar flux multiplied by the

time-averaged null depth of the interferometer  $\bar{N}$ . This quantity determines what part of the stellar flux leaks into the telescope due to the finite extent of the star (the entire star cannot be perfectly in the line of sight of the telescope) and the alignment errors of the telescope. It can be calculated as follows:

$$\bar{N} = \frac{1}{4} \left[ \sigma_\phi^2 + \frac{\pi^2}{4} \left( \frac{\theta_{\text{dia}}}{\lambda_{\text{sh}}/b} \right)^2 + \sigma_I^2 \right], \quad (5)$$

whereby  $\theta_{\text{dia}}$  denotes the star angular diameter,  $\sigma_I^2$  the variance of the fractional intensity deviations (which arises from errors in the tip and tilt angles of the telescope) and  $\sigma_\phi^2$  the variance of the phase error (which arises due to errors in the optical path difference). See [8] for a derivation of this formula as well as [7] for a detailed discussion on  $\sigma_I^2$  and  $\sigma_\phi^2$ .

The instrumental nulling noise is noise due to the imperfect construction of the telescope. As is shown in [8], it is the product of the OSF and  $\sigma_N$  with

$$\sigma_N = \sqrt{\frac{\sigma_\phi^4 + \sigma_I^4}{8}}. \quad (6)$$

## 2.4 Signal-to-Noise ratio and integration time

The crucial quantity which determines whether or not an exoplanet can be detected is the integration time  $t_i$ . It can be calculated as follows:

$$t_i = \left( \frac{\text{SNR}_{\text{req}}}{\text{SNR}_{1s}} \right)^2 = \left( \frac{5}{\text{SNR}_{1s}} \right)^2, \quad (7)$$

where  $\text{SNR}_{\text{req}}$  is the minimal required signal-to-noise ratio and is fixed to 5.

The signal to noise ration generated in 1 second can be expressed as (neglecting the detector noise)

$$\text{SNR}_{1s} = \frac{\text{OPF}}{\sqrt{(N_s^2 + N_{\text{inst}}^2)}}. \quad (8)$$

## 3 Results

### 3.1 Overview

Using the model described in the section above, I calculated the integration times for 36 of the 49 previously directly imaged planets according to the NASA Exoplanet Archive ([4]). The data for the exoplanets and their host stars are obtained from the database where available. In some cases, the exoplanet temperature or radius is not known; for these,

	Integration times (in s)		
	CubeSat6U	CubeSat12U	PROBA
HIP 65426 b	179.372	152.330	8.447
USco CTIO 108 b	58.795	63.506	inf
2MASS J01225093 2439505 b	1.455	1.396	1.034
2MASS J22362452+4751425 b	15.823	17.233	inf
kap A b	1.675	0.992	0.084
GSC 06214 00210 b	1.453	1.570	inf
1RXS J160929.1-210524 b	14.064	13.100	inf
HN Peg b	inf	inf	inf
HD 203030 b	inf	inf	inf
GQ Lup b	0.554	0.627	0.045
HD 100546 b	12.586	39.309	1.672
2MASS J04414489+2301513 b	7.000E+16	1.880E+16	9.221E+14
Fomalhaut b	inf	inf	inf
ROXs 12 b	1.524E+18	1.867E+18	1.126E+19
PDS 70 b	91.331	14.539	1.304
PDS 70 c	470.093	230.944	32.142
Oph 11 b	0.863	0.941	15.887
HR 8799 b	142.224	125.517	22.999
HR 8799 c	149.838	99.379	6.189
HR 8799 d	22.061	95.251	2.906
HR 8799 e	86.943	132.893	8.854
HIP 78530 b	186.814	200.513	inf
HD 95086 b	1287.764	9187.373	151.443
HD 106906 b	1.003E+04	1.082E+04	inf
GJ 504 b	3.033E+04	5.132E+04	inf
2MASS J12073346-3932539 b	14.431	21.866	0.818
AB Pic b	3.477E+10	4.796E+10	inf
bet Pic b	0.284	1.004	0.047
CFBDSIR J145829+101343 b	2.720E+09	1.837E+08	3.780E+04
CHXR 73 b	5.237E+19	5.814E+19	1.708E+18
CT Cha b	2.159	2.376	inf
DH Tau b	0.997	0.901	inf
GU Psc b	inf	inf	inf
WISEP J121756.91+162640.2 A b	1.729E+04	1.819E+04	381.629
2MASS J02192210-3925225 b	1.060	1.163	inf
TYC 8998-760-1 b	1.441	1.644	6.317

Table 2: Integration times (in s) for 36 previously directly imaged exoplanets for  $\sigma_{OPD} = 10nm$  and  $\sigma_{Tip/Tilt} = 300mas$  and optimal wavelength.



	Optimal wl	OPF (ph/s)	OSF (ph/s)	OBF (ph/s)	SNR 1s	$t_{int}$ (s)
<b>CubeSat 6U</b>	$2.88\mu m$	150	1277	85	3.86	1.675
<b>CubeSat 12U</b>	$3.18\mu m$	195	758	561	5.02	0.992
<b>PROBA</b>	$3.48\mu m$	1652	4628	2876	17.26	0.084

Table 3: Radiometric budget for Kap A b. The output planet flux is at worst one order of magnitude smaller than the other sources, which leads to very short integration times.

the temperature was approximated using the Stefan-Boltzmann law and the radius was approximated by assuming the exoplanet has a density equal to that of Jupiter. For 13 of the exoplanets, other crucial datapoints were unavailable and they were therefore left out of the analysis.

Furthermore, platform stability parameters of  $\sigma_{OPD} = 10nm$  and  $\sigma_{Tip/Tilt} = 300mas$  were chosen. The wavelength at which the exoplanet is to be detected is not predefined but rather optimized, i.e. the model calculates which wavelength in the range from  $0.5 - 30\mu m$  leads to the shortest integration time.

Table 2 shows the resulting integration times for each of the three telescope configurations. Note that for some configurations, the exoplanet system is wider than the outer working angle ( $OWA = 0.514 \cdot \frac{\lambda}{D}$ , where  $\lambda_{max} = 5\mu m$  was chosen, as larger wavelengths do not produce good results anymore). These are denoted with an infinite integration time.

It can be seen immediately that according to this model, it is indeed possible to detect certain exoplanets within a matter of seconds using the Bracewell interferometer setup. To understand why, it helps to take a closer look at the measured incoming fluxes. As an example, the OPF, OSF and OBF as described in section 2 are listed in Table 3 for Kap A b. The OPF is between the same and one order of magnitude smaller than the other sources and therefore it is not surprising that the exoplanet can be detected almost instantly.

### 3.2 Differences between configurations

A quick note regarding the difference in integration times between the telescopes. Intuitively one would expect that the larger the telescope in terms of baseline length and lens diameter, the shorter the required integration time. This is indeed true for most cases, but there are a few exceptions, as for example TYC 8998-760-1 b. The reason for the CubeSat 6U having a smaller  $t_{int}$  than the 12U is that the transmission function for a given setup is periodic (see Figure 1). The baseline of the CubeSats are not adjustable and in the case of TYC 8998-760-1 b the transmission function is significantly greater for  $b = 0.5m$  than  $b = 1m$ , overcompensating the other positive effects of the larger baseline

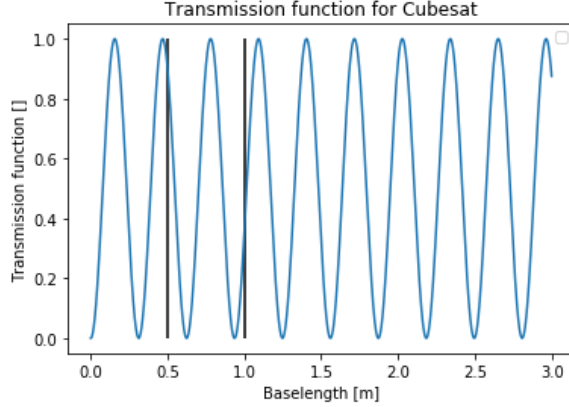


Figure 5: Transmission function for TYC 8998-760-1 b for the CubeSat setup with variable baseline length.

(Figure 5).

The PROBA telescope on the other hand suffers from the fact that its large lens diameter allows for a maximum operating wavelength of  $4.04\mu m$ , as otherwise the exoplanet is outside the outer working angle. This is around  $1.5\mu m$  larger than the otherwise optimal wavelength and explains why it performs worse than both of the CubeSat configurations.

### 3.3 Impact of platform stability constraints

As a final point of interest the dependencies of the platform stability parameters  $\sigma_{OPD}$  and  $\sigma_{Tip/Tilt}$  were analysed. To this end, I increased both the parameters by a factor of 10 and recalculated the integration times in separate runs. The results are shown in Figure 6. It can be seen that increase of  $\sigma_{Tip/Tilt}$  had a much greater effect. While the adjusted  $\sigma_{OPD}$  led to an increase in  $t_{int}$  of around one order of magnitude, the same increase in  $\sigma_{Tip/Tilt}$  resulted in increases in  $t_{int}$  of around three orders of magnitude.

## 4 Discussion

### 4.1 Incoming fluxes

To verify the results presented in the chapter above, I will compare the output of this model to that of Colin Dandumont (referred to as Colin’s model from here on), which is described in [7] and [5]. The models were implemented independently of each other except where noted otherwise.

The first numbers of interest are the incoming fluxes from the various sources. Figures 7–8 show a comparison between the two models for a synthetic planet around Proxima

	Integration times (in s)								
	$\sigma_{OPD} = 10nm, \sigma_{TipTilt} = 300mas$			$\sigma_{OPD} = 100nm, \sigma_{TipTilt} = 300mas$			$\sigma_{OPD} = 10nm, \sigma_{TipTilt} = 3000mas$		
	CubeSat6U	CubeSat12U	PROBA	CubeSat6U	CubeSat12U	PROBA	CubeSat6U	CubeSat12U	PROBA
HIP 65426 b	179.372	152.33	8.447	1408.726	2005.102	150.112	2.47E+06	1.19E+07	3.35E+05
USco CTIO 108 b	58.795	63.506	inf	58.847	63.562	inf	4556.229	3822.208	inf
2MASS J01225093 2439505 b	1.455	1.396	1.034	6.611	6.269	1.173	9.62E+04	5.25E+04	2798.5
2MASS J22362452+4751425 b	15.823	17.233	inf	87.581	89.483	inf	1.96E+05	2.13E+05	inf
kap A b	1.675	0.992	0.084	46.765	21.762	2.776	3.26E+04	2.88E+05	5700.798
GSC 06214 00210 b	1.453	1.57	inf	7.285	7.255	inf	1.51E+05	1.00E+05	inf
1RXS J160929.1-210524 b	14.064	13.1	inf	90.089	92.642	inf	8.89E+05	9.27E+05	inf
HN Peg b	inf	inf	inf	inf	inf	inf	inf	inf	inf
HD 203030 b	inf	inf	inf	inf	inf	inf	inf	inf	inf
GQ Lup b	0.554	0.627	0.045	1.841	2.54	0.268	2.14E+04	5.01E+04	4553.302
HD 100546 b	12.586	39.309	1.672	110.485	196.586	13.87	3.59E+05	7.90E+04	7827.455
2MASS J04414489+2301513 b	7.00E+16	1.88E+16	9.22E+14	2.13E+17	4.59E+16	6.23E+15	6.57E+22	5.12E+21	3.13E+20
Fomalhaut b	inf	inf	inf	inf	inf	inf	inf	inf	inf
ROXs 12 b	1.52E+18	1.87E+18	1.13E+19	1.68E+19	1.78E+19	1.25E+19	2.92E+24	1.02E+24	8.45E+22
PDS 70 b	91.331	14.539	1.304	704.608	89.203	14.204	1.82E+07	1.42E+06	4.89E+04
PDS 70 c	470.093	230.944	32.142	3053.978	1137.055	215.037	2.78E+07	3.26E+06	2.93E+05
Oph 11 b	0.863	0.941	15.887	0.915	1	15.89	2022.961	2069.143	222.191
HR 8799 b	142.224	125.517	22.999	1817.712	1460.554	112.143	2.16E+06	2.79E+06	1.27E+05
HR 8799 c	149.838	99.379	6.189	1065.052	1805.102	120.783	9.50E+05	3.80E+06	1.13E+05
HR 8799 d	22.061	95.251	2.906	232.528	1186.852	61.073	1.73E+06	5.89E+05	6.89E+04
HR 8799 e	86.943	132.893	8.854	1172.526	969.304	199.65	1.23E+07	1.66E+06	1.73E+05
HIP 78530 b	186.814	200.513	inf	190.205	204.153	inf	1.40E+05	1.62E+05	inf
HD 95086 b	1287.764	9187.373	151.443	9362.146	5.73E+04	1.73E+03	1.70E+07	1.08E+07	1.01E+06
HD 106906 b	1.00E+04	1.08E+04	inf	1.00E+04	1.08E+04	inf	7.11E+05	6.41E+05	inf
GJ 504 b	3.03E+04	5.13E+04	inf	2.34E+05	2.22E+05	inf	1.91E+07	1.17E+07	inf
2MASS J12073346-3932539 b	14.431	21.866	0.818	22.244	45.957	1.619	2.65E+04	1.40E+05	4006.762
AB Pic b	3.48E+10	4.80E+10	inf	3.56E+10	4.85E+10	inf	4.39E+10	6.00E+10	inf
bet Pic b	0.284	1.004	0.047	7.052	10.824	2.052	1.29E+05	1.88E+04	2245.377
CFBDSIR J145829+101343 b	2.72E+09	1.84E+08	3.78E+04	2.72E+09	1.84E+08	3.78E+04	4.89E+09	3.26E+08	1.27E+05
CHXR 73 b	5.24E+19	5.81E+19	1.71E+18	1.90E+20	2.05E+20	1.50E+19	7.15E+24	7.09E+24	6.74E+23
CT Cha b	2.159	2.376	inf	11.897	12.603	inf	2.21E+05	2.41E+05	inf
DH Tau b	0.997	0.901	inf	4.385	4.793	inf	5.80E+04	6.11E+04	inf
GU Psc b	inf	inf	inf	inf	inf	inf	inf	inf	inf
WISEP J121756.91+162640.2 A b	1.73E+04	1.82E+04	381.629	1.73E+04	1.82E+04	383.797	5.11E+04	4.36E+05	6640.64
2MASS J02192210-3925225 b	1.06	1.163	inf	1.341	1.477	inf	7951.732	7382.429	inf
TYC 8998-760-1 b	1.441	1.644	6.317	8.688	8.15	6.495	1.84E+05	6.68E+04	5028.455

Figure 6: Analysis of the effect of platform stability parameters. The first three columns show  $t_{int}$  for  $\sigma_{OPD} = 10nm$  and  $\sigma_{TipTilt} = 300mas$ , the next three for  $\sigma_{OPD}$  increased by a factor of 10 and the final three for  $\sigma_{TipTilt}$  increased by a factor of 10.

Centauri for varying wavelength. It can be seen that the curves of the fluxes from Proxima Centauri, the exoplanet and the local zodiacal dust are almost identical. The curve for the thermal emission is similar, but this means nothing as the geometry factor described in chapter 2 was chosen in such a fashion to fit the plot. Finally, the curve for exozodiacal dust is missing in my model for the reasons explained.

In a similar direction goes the comparison of the planet flux, the noise contributions as well as the signal-to-noise ratio as a function of varying wavelength. This is shown in Figures 9-11 for the same synthetic planet as before. One can see that the behaviour is again very similar, especially at low wavelengths. At wavelengths  $> 10\mu m$  it appears that all three components (planet flux, shot noise and instrumental noise) are lower in my model compared to Colin's. I have no explanation to offer for this effect; however, fortunately

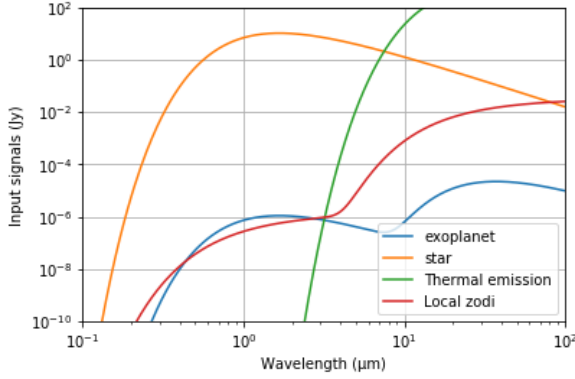


Figure 7: Incoming fluxes as described by the model used in this paper.

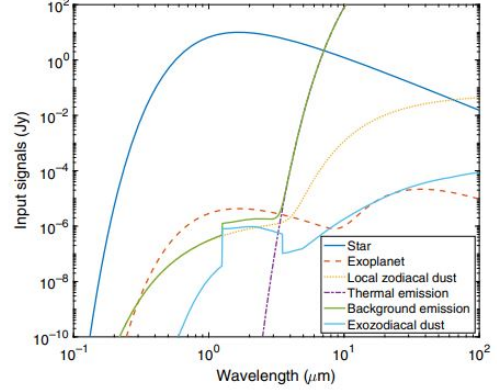


Figure 8: Incoming fluxes as described by the model used in [7].

the optimal wavelength for all of the exoplanets is between  $1 - 5\mu m$ .

## 4.2 Results for nearby exoplanets

The next step is to compare not only the incoming fluxes but also the resulting integration times, which is the ultimate figure of interest. In [5], the integration times for the nearest known exoplanets are evaluated (see [5] for their parameters). Figure 12 in the Appendix shows the results calculated using my model as opposed to Figure 13, which are the results from Colin's model. It can be seen that with a few exceptions the results do not differ by more than a factor of 2. Note that platform stability constraints were not considered (i.e.  $\sigma_{OPD} = \sigma_{Tip/Tilt} = 0$ ) and the integration times are given in hours; clearly the nearest exoplanets are much harder to detect than those analysed in this paper.

## 4.3 Results for directly imaged exoplanets

As described in the last chapter, my model predicts that many of the analysed exoplanets can be detected within a matter of seconds. This is a key result and therefore I asked Colin Dandumont to run his model on a selection of the directly imaged planets also. The results for 2MASS J01225093 2439505 b (abbr. 2Mass), bet Pic b, HD 95086 (abbr. HD), kap A b and TYC 8998-760-1 b (abbr. TYC) are depicted in the appendix (Figures 14 to 43). Platform stability parameters of  $\sigma_{OPD} = 10nm$  and  $\sigma_{TipTilt} = 300mas$  were used for all calculations.

Overall, it can be confirmed that all of the planets considered can be detected within very reasonable time. It can generally be said that Colin's model predicts smaller integration times (no more than a factor of 5) for the CubeSat configurations, while my model predicts smaller ones for the PROBA telescope. Unfortunately, I have no meaningful explanation

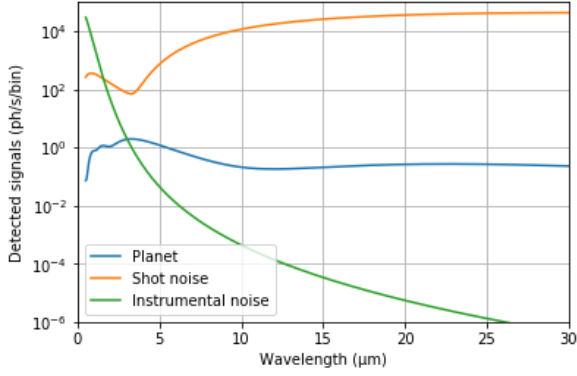


Figure 9: Incoming fluxes as described by the model used in this paper.

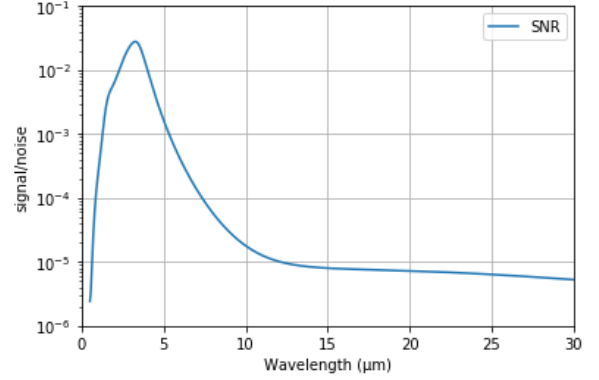


Figure 10: Signal-to-Noise ratio as described by the model used in this paper.

to offer for this discrepancy.

Of special note is the plot my model produces for TYC 8998-760-1 b and 2MASS J01225093 2439505 b using the PROBA telescope. Theses plots differs strongly from the ones using the other model and seem to predict too small an integration time compared to with the CubeSat configurations.

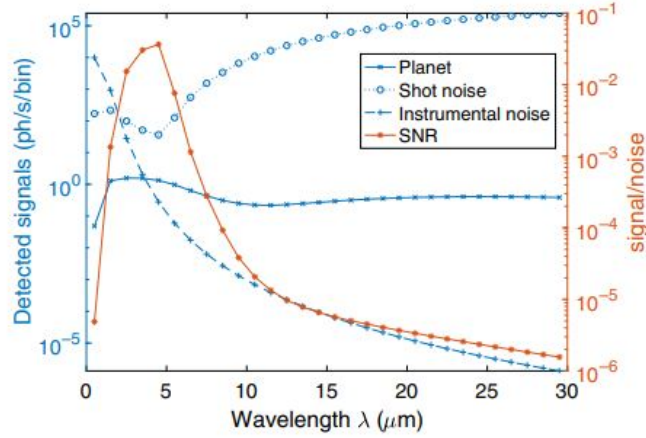


Figure 11: Incoming fluxes and Signal-to-Noise ratio as described by Colin's model.

## 5 Conclusion

The key question of this project was to determine if a small satellite configuration could detect known, previously detected exoplanets in a reasonable amount of time using the Bracewell interferometer setup. According to the model implemented and backed up by

the model described in [5], it has been shown that this is indeed possible, as many of these exoplanets can be detected in a matter of seconds or minutes.

The next steps in demonstrating the feasibility of the proof-of-concept mission would be to first include estimations for exozodiacal dust emission in the model, as this can be significant if a large exozodiacal disk surrounds the targeted exoplanet. Additionally, some simplifications have been made regarding the functioning of the telescope, for example neglecting any global tip-tilt mis-alignment if the telescope does not point perfectly at the star. It should be confirmed that the slight offsets that must be expected can indeed be neglected or else that error also included in the calculation. Similarly, it must be shown that the platform stability parameters of  $\sigma_{OPD} = 10nm$  and  $\sigma_{TipTilt} = 300mas$  are indeed feasible from an engineering standpoint (the telescope must not only be constructed with these specifications but also survive the trip into orbit), as we have seen that especially the differential tip/tilt has a great impact on the result. Finally, the discrepancy in integration time between this model and Colin's model for TYC 8998-760-1 b and 2MASS J01225093 2439505 b using the PROBA telescope should be understood; to this end, it would be helpful to compare the models for a larger number of planets and analyse if there is a pattern where this discrepancy is found.

# Appendices

Figures 12 and 13 show the integration times for the nearest known exoplanets as calculated by my model compared to Colin's.

	Integration time (h)				Integration time (h)		
	CubeSat6U	CubeSat12U	PROBA		CubeSat6U	CubeSat12U	PROBA
Proxima centauri b	2E+03	193	12	eps Ind A b	inf	inf	inf
Proxima centauri c	2E+05	3E+05	inf	tau Cet e	576	958	6.E+03
Barnard's star b	5.E+03	3.E+04	2.E+04	tau Cet f	27098	131976	3.E+05
Wolf 359 b	8.E+05	7.E+05	inf	tau Cet g	1.E+03	249	12
Wolf 359 c	5.E+04	3.E+03	1	tau Cet h	1.E+03	336	719
Lalande 21185 b	698	111	7	GJ1061 b	3.E+06	2.E+05	13
eps Eridani b	929	4.E+03	inf	GJ1061 c	2.E+06	1.E+05	12
GJ887 b	2.E+03	226	3	GJ1061 d	2.E+06	1.E+05	15
GJ887 c	201	30	6	GJ273 b	6.E+04	5.E+03	22
Ross 128	4.E+05	3.E+04	10	GJ273 c	2.E+05	1.E+04	9
GJ 15A b	1.E+04	1.E+03	6	GJ273 d	4.E+03	8.E+03	4.E+03
YZ Cet b	7.E+06	4.E+05	28	GJ273 e	7.E+03	3.E+04	7.E+03
YZ Cet c	4.E+06	3.E+05	19	Teegarden's star b	1.E+08	8.E+06	184
YZ Cet d	4.E+06	3.E+05	21	Teegarden's star c	1.E+08	8.E+06	211

Figure 12: Integration times for the nearest known exoplanets calculated using my model. The parameters used are  $\lambda = 1.5\mu m$ ,  $T = 150K$  and  $\sigma_{OPD} = \sigma_{TipTilt} = 0$ . The planet parameters can be found in [5].

	Integration time (h)				Integration time (h)		
	CubeSat 6U	CubeSat 12U	PROBA-size		CubeSat 6U	CubeSat 12U	PROBA-size
Proxima Centauri b	3e+03	273	12	eps Ind A b	Inf	Inf	Inf
Proxima Centauri c	2e+05	3e+05	Inf	tau Cet e	7e+02	2e+03	9e+03
Barnard's star b	1e+04	3e+04	1e+04	tau Cet f	3e+04	1e+05	3e+05
Wolf 359 b	1e+06	1e+06	3e+06	tau Cet g	1e+03	264	76
Wolf 359 c	1e+05	7e+03	1	tau Cet h	1e+03	375	1e+03
Lalande 21185 b	1e+03	149	10	GJ 1061 b	8e+06	5e+05	18
eps Eridani b	1e+03	4e+03	Inf	GJ 1061 c	6e+06	4e+05	16
GJ 887 b	2e+03	249	3	GJ 1061 d	7e+06	4e+05	26
GJ 887 c	152	19	3	GJ 273 b	1e+05	8e+03	17
Ross 128 b	9e+05	6e+04	10	GJ 273 c	4e+05	3e+04	10
GJ 15A b	2e+04	2e+03	5	GJ 273 d	9e+03	2e+04	4e+03
YZ Cet b	9e+06	6e+05	29	GJ 273 e	2e+04	5e+04	9e+03
YZ Cet c	5e+06	3e+05	16	Teegarden's star b	2e+08	1e+07	290
YZ Cet d	5e+06	3e+05	18	Teegarden's star c	2e+08	1e+07	343

Figure 13: Integration times for the nearest known exoplanets calculated using Colin's model. The parameters used are  $\lambda = 1.5\mu m$ ,  $T = 150K$  and  $\sigma_{OPD} = \sigma_{TipTilt} = 0$ . The planet parameters can be found in [5].

The following figures 14-43 show the integration times as a function of wavelength for the CubeSat 6U, CubeSat 12U and PROBA configurations.

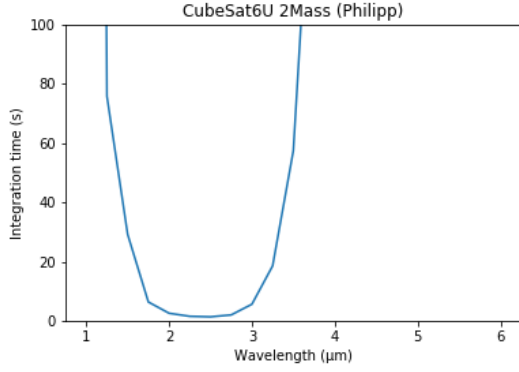


Figure 14: Integration times calculated by the model described in this report.

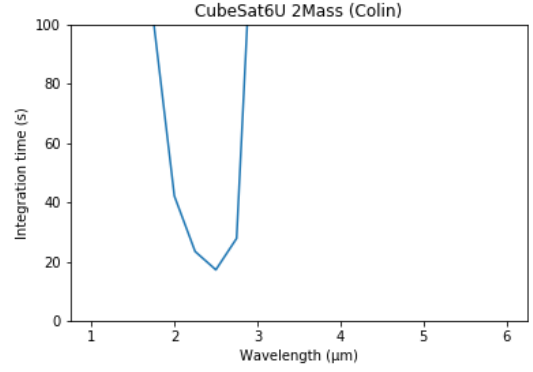


Figure 15: Integration times calculated by the model described in [7].

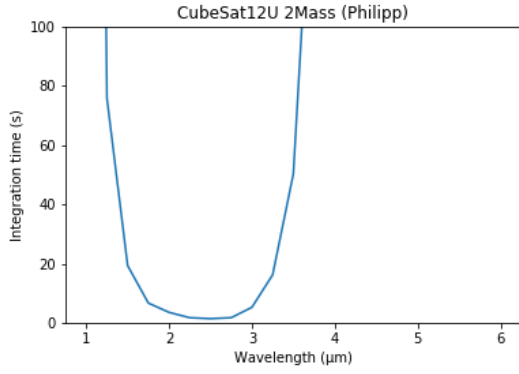


Figure 16: Integration times calculated by the model described in this report.

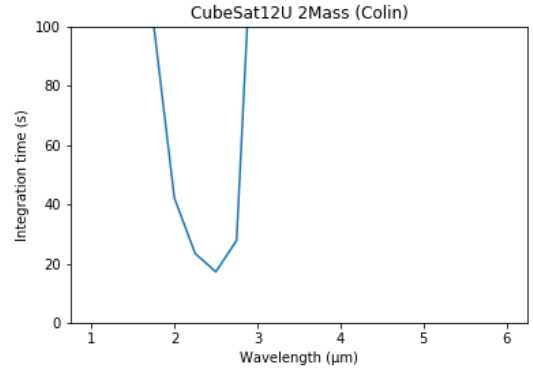


Figure 17: Integration times calculated by the model described in [7].

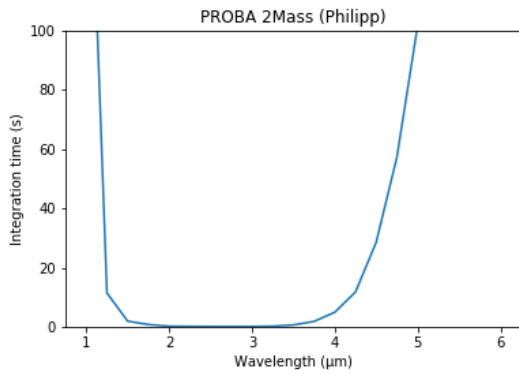


Figure 18: Integration times calculated by the model described in this report.

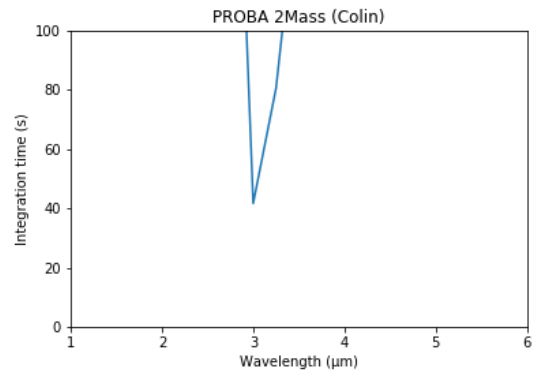


Figure 19: Integration times calculated by the model described in [7].



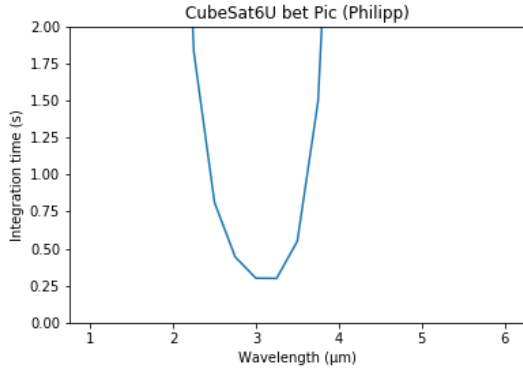


Figure 20: Integration times calculated by the model described in this report.

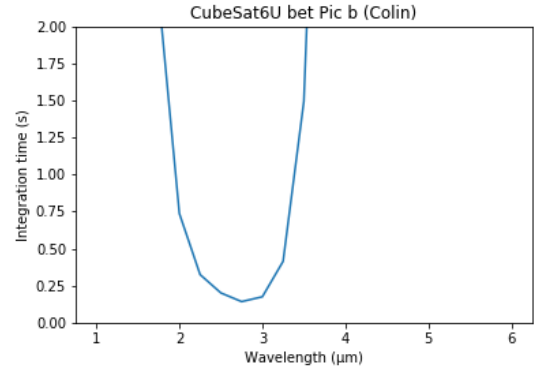


Figure 21: Integration times calculated by the model described in [7].

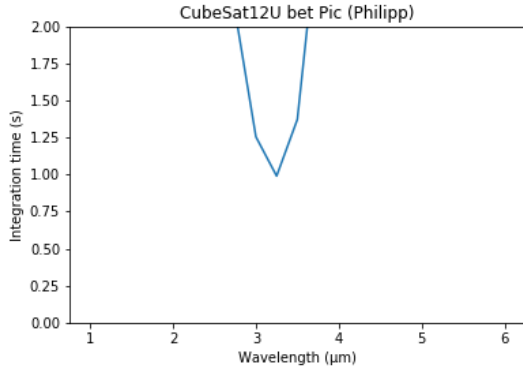


Figure 22: Integration times calculated by the model described in this report.

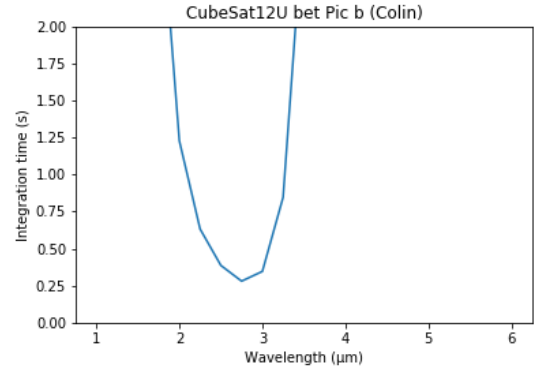


Figure 23: Integration times calculated by the model described in [7].

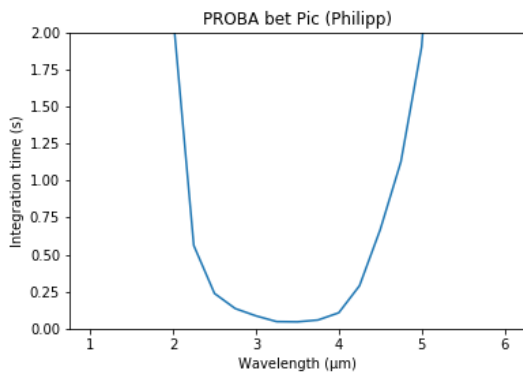


Figure 24: Integration times calculated by the model described in this report.

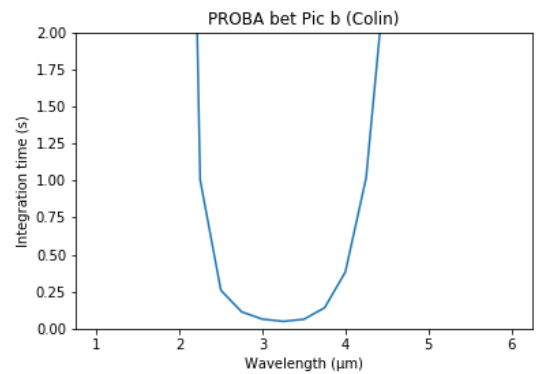


Figure 25: Integration times calculated by the model described in [7].

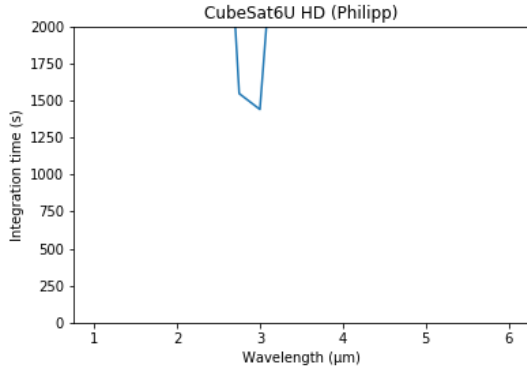


Figure 26: Integration times calculated by the model described in this report.

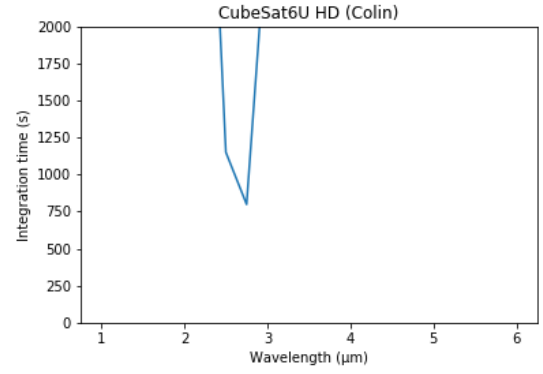


Figure 27: Integration times calculated by the model described in [7].

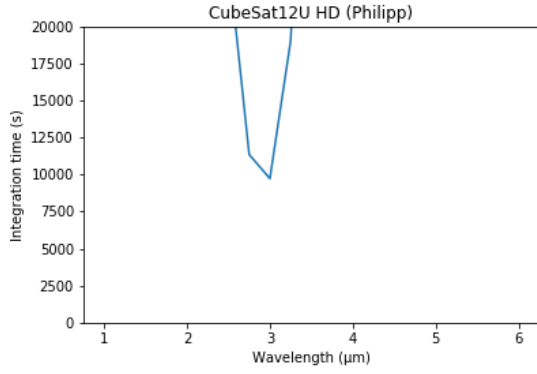


Figure 28: Integration times calculated by the model described in this report.

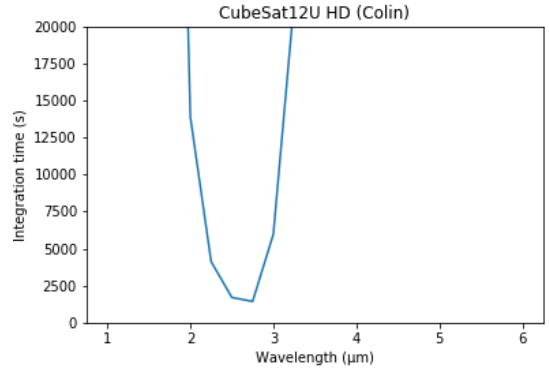


Figure 29: Integration times calculated by the model described in [7].

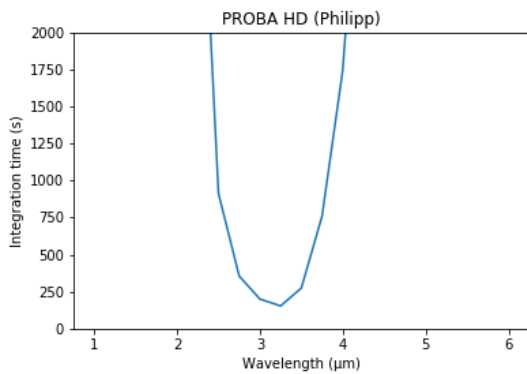


Figure 30: Integration times calculated by the model described in this report.

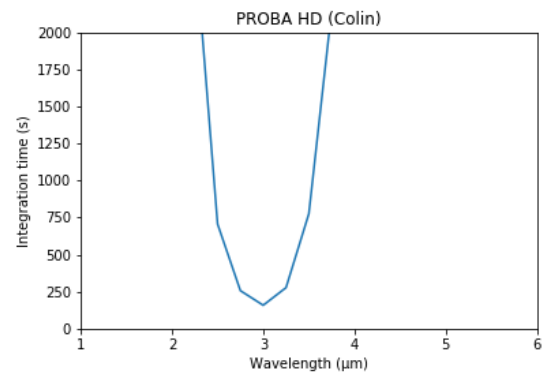


Figure 31: Integration times calculated by the model described in [7].

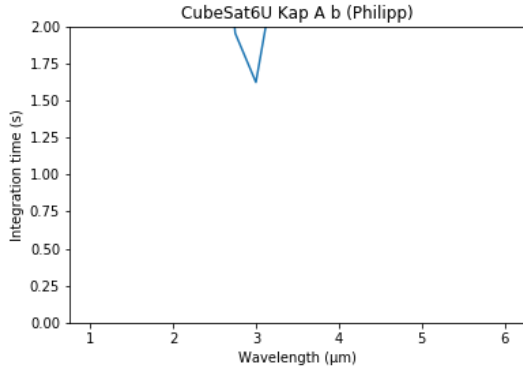


Figure 32: Integration times calculated by the model described in this report.

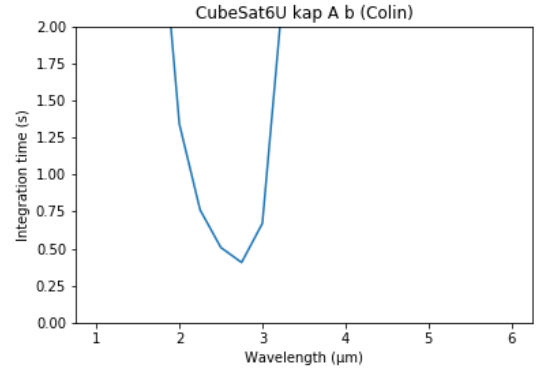


Figure 33: Integration times calculated by the model described in [7].

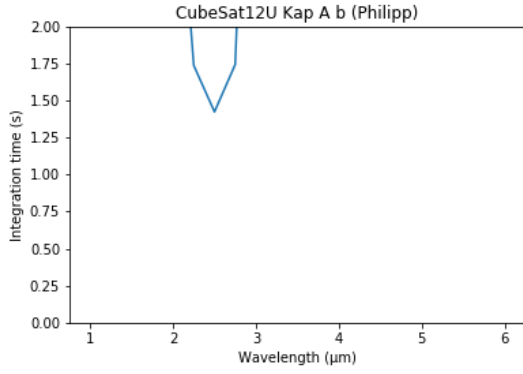


Figure 34: Integration times calculated by the model described in this report.

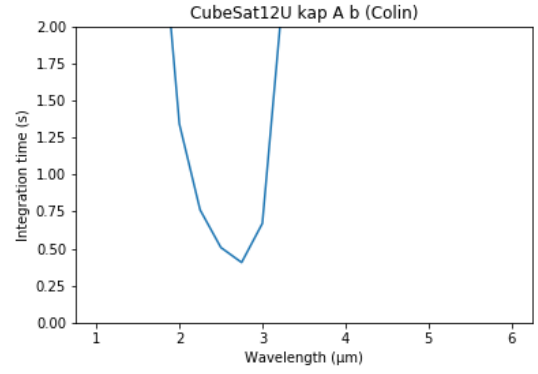


Figure 35: Integration times calculated by the model described in [7].

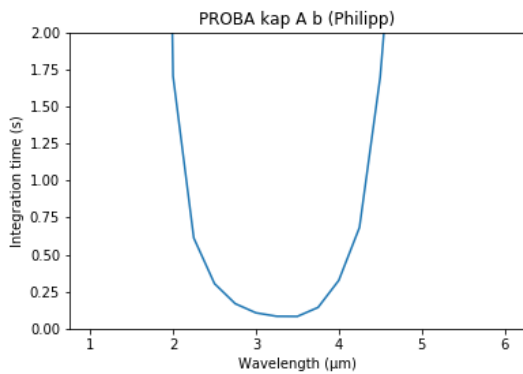


Figure 36: Integration times calculated by the model described in this report.

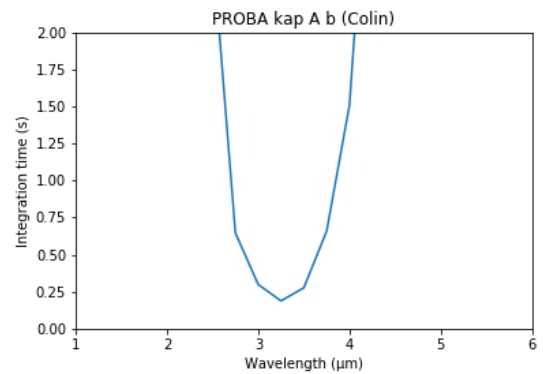


Figure 37: Integration times calculated by the model described in [7].

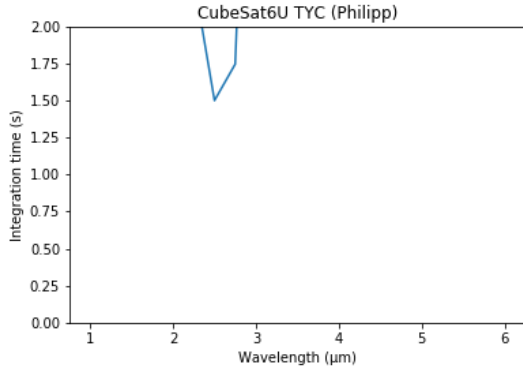


Figure 38: Integration times calculated by the model described in this report.

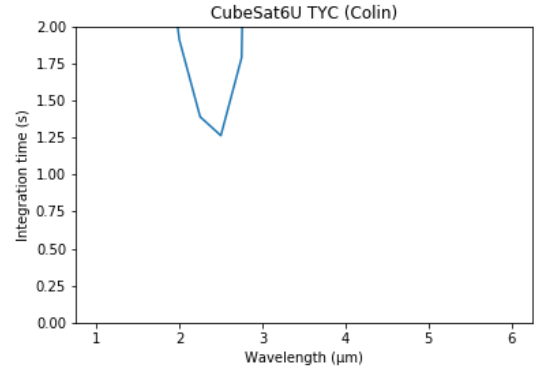


Figure 39: Integration times calculated by the model described in [7].

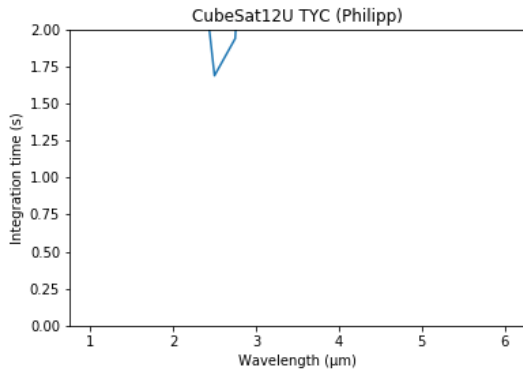


Figure 40: Integration times calculated by the model described in this report.

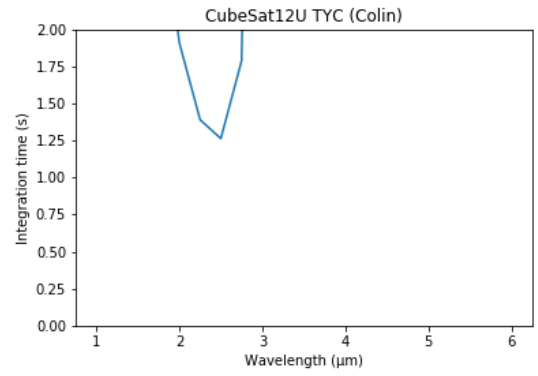


Figure 41: Integration times calculated by the model described in [7].

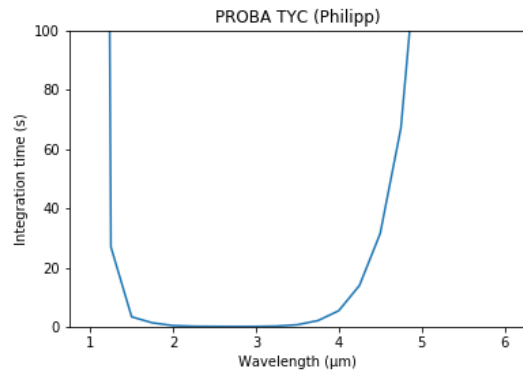


Figure 42: Integration times calculated by the model described in this report.

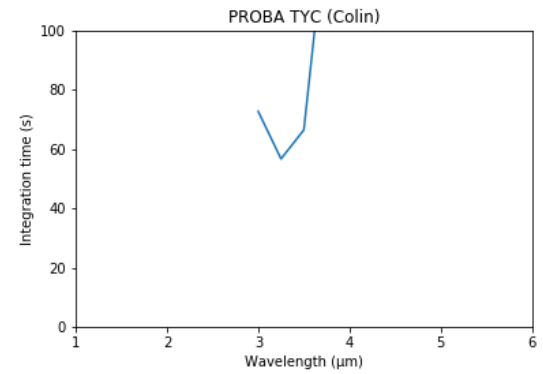


Figure 43: Integration times calculated by the model described in [7].

## References

- [1] Rouan D: "Nulling Interferometry", in [Gargaud M. et al. (eds) Encyclopedia of Astrobiology. Springer, Berlin, Heidelberg]. (2011)
- [2] Hinz, P. M., Angel, J. R. P., Woolf, N. J., Hoffmann, W. F., and McCarthy, D. W.: "Imaging Extra-solar Systems from the Ground: The MMT and LBT Nulling Interferometers", in [Working on the Fringe: Optical and IR Interferometry from Ground and Space 194, 401]. (1999)
- [3] Quanz, S. P., Kammerer, J., Defrère, D., Absil, O., Glauser, A. M., and Kitzmann, D: "Exoplanet science with a space-based mid-infrared nulling interferometer" in [Optical and Infrared Interferometry and Imaging VI, 10701, 107011I, International Society for Optics and Photonics]. (2018)
- [4] Website: <https://exoplanetarchive.ipac.caltech.edu>
- [5] Colin Dandumont, Jens Kammerer, Denis Defrère, Jérôme Loicq: "Performance study of interferometric small-sats to detect exoplanets: Updated exoplanet yield and application to nearby exoplanets". (2020)
- [6] Maurice Ottiger, Sascha P. Quanz, Felix Dannert, Adrian Gheorghe, Emile Fontanet, Olivier Absil, Colin Dandumont, Denis Defrère, Carlos Gascón, Adrian Glauser, Jens Kammerer, Romain Laugier, Tim Lichtenberg, Jérôme Loicq, and the LIFE collaboration: "Large Interferometer For Exoplanets (LIFE): II. Signal simulation, signal extraction and fundamental exoplanet parameters from single epoch observations". (2021)
- [7] Colin Dandumont, Denis Defrère, Jens Kammerer, Olivier Absil, Sascha P. Quanz, Jérôme Loicq: "Exoplanet detection yield of a space-based Bracewell interferometer from small to medium satellites". (2020)
- [8] E. Serabyn: "Nulling interferometry: symmetry requirements and experimental results", in [Proc. SPIE 4006, 328]. (2000)